Flow Field Characteristics of Oblique Shocks Generated Using Microjet Arrays

Mohd Y. Ali[1], Farrukh S. Alvi[1], Rajan Kumar[1] and Kareem A. Ahmed[2]
[1]Department of Mechanical Engineering, Florida Center for Advanced Aero-Propulsion (FCAAP), Florida State University, Tallahassee, FL 32310
[2]Department of Mechanical and Aerospace Engineering, Old Dominion University, Norflok, VA 23529

Received date: 8/12/2014; Accepted date: 10/7/2014

ABSTRACT
High-momentum steady microjet arrays are used to generate single and/or multiple oblique shocks in a supersonic crossflow. The properties of these microjet-generated shocks can be tailored to be parallel or coalescing, depending on the application, by adjusting the pressure ratio. Building upon the results of prior studies, flow field measurements using Particle Image Velocimetry were obtained. The velocity field clearly shows the effect of the microjet-generated oblique shocks on the flow field. Changes in the velocity field across the oblique shock and the expansion fan are also clearly seen from these results. The strength of the microjet-generated shocks was found to be constant along the length of the shock. Properties of microjet-generated shocks are compared with oblique shocks using a ramp and differences and similarities between the two are found. Flow properties due to multiple parallel and coalescing shocks were also investigated to better understand the behavior of such flow features introduced using fluidic micro-actuators.

1. INTRODUCTION

Jet injection in supersonic crossflow has been a problem of interest for researchers over the last few decades, due to its complex fundamental flow physics and wide range of applications. Studies on the evolution and interaction of a jet in supersonic crossflow have been well documented in the literature [1–2]. Subsequent studies have helped in further understanding of this complex flow field (Ben-Yakar et al. [3]) and in developing flow control devices based on these fundamental principles. Mahesh [4] provides a recent, comprehensive review of single jets in crossflow. Some applications of jet injection include fuel injectors in scramjets [5–6], active flow control of cavities in supersonic flow using micro-orifice jets [7–8], suppression of jet noise in high-speed flows among others (Alvi et al. [9]). Interaction of the injectant with the supersonic crossflow creates a shock wave, where a sufficiently strong shock wave (due to high injection pressures or momentum flux) is capable of separating the incoming boundary layer. Associated with the shock wave produced due to jet injection are regions of fluid recirculation both upstream and downstream of the shock wave. As the injectant penetrates into the boundary layer, both small and large-scale structures evolve into the boundary layer, changing its characteristics. The formation of a shock wave is ubiquitously followed by an expansion fan to turn the flow back to its original direction as dictated by the boundary condition. The formation of the shock wave and its interaction with the surface boundary layer is commonly known as a shock wave – boundary layer interaction (SBLI). The problem of SBLI, although well documented is still an active area of research [10–15] due to its complexity and vast applications. A fundamental understanding of the jets injected into the supersonic crossflow has helped in simplifying these highly complex flow phenomena with some success, and if appropriately developed may also be instrumental in designing novel flow control devices and techniques to mitigate some of the adverse effects typically associated with SBLI such as flow unsteadiness, inlet buzz/unstart, and sonic boom mitigation among others. Some of these problems and prior approaches to their solution are briefly discussed next.

The concept of body shaping dates back to 1950's when NACA research engineers worked on designing aircraft with a smooth cross-sectional area distribution, which led to a reduction of the peak drag near Mach 1. Recent studies focus on tailoring shock waves to achieve desired compression of the incoming flow. Gulfstream's quiet spike program (Howe et al. [16]) uses a long telescopic fuselage extension to alter the N-wave pressure signature by breaking down the strong bow shock in front of the canopy into a series of weaker shock waves upstream of the fuselage such that the terminal bow shock becomes weaker. The fuselage extension employed also ensures that these weaker shocks remain parallel in the farfield, hence not coalesce to avoid the possibility of a sonic boom. Another problem that continues to pose a technological challenge is that of the supersonic air inlets. Although the geometry of some of the supersonic inlets can be simple, the flow field in and around the inlet is highly complex. Incoming flow interacts with the inlet surfaces producing multiple shock systems that further interact with the inlet boundary layer. The interaction of the shock system with the boundary layer causes: flow unsteadiness, loss of total pressure recovery, flow distortion at the inlet-engine interface, local or, in severe cases global separation etc., thereby severely degrading inlet performance. Thus, control of SBLI can prove instrumental in improving the efficiency of supersonic inlets for the next generation of aircraft and possibly developing a viable solution for a future commercial supersonic transport.

Recently, studies have also focused on employing passive devices such as vortex generators and active devices capable of steady and unsteady forcing of the SBLI using vortex generators jets. Valdivia et al. [17] have experimented with Wheeler Doublets (WDs) vortex generators, vortex generator jets (VGJs) and their combination on supersonic inlet unstart at Mach 5. The results showed that the combination of WDs and VGJs proved effective in delaying unstart of the inlet. Anderson et al. [18] developed a hybrid technique combining micro-vanes, micro-ramps and micro-jets for flow control over the vehicle forebody and serpentine inlet systems. There study showed that injecting small amount of high-pressure air using the micro-jets into the vortex generated by the micro-vanes and micro-ramps provides substantial augmentation and active flow control on the flow field. Another novel technique employing high-momentum microjet arrays capable of generating single and/or multiple oblique shocks of varying strengths that can be either parallel or coalescing depending on the application has been the subject of study at the Florida Center of Advanced Aero-Propulsion (FCAAP) at Florida State University. Previous studies (Kumar et al. [19]) employing flow visualization and density field measurements using Background Oriented Schlieren (BOS) have shown that the microjet-generated shocks are capable of decelerating and turning the flow through oblique shocks, and thus show promise of augmenting conventional ramps for flow compression.

The present study explores the flow characteristics of microjet-generated shocks using flow visualization and detailed velocity field measurements using PIV. Active control of the shock wave strength by varying the supply pressure to the microjet arrays, and its impact on the overall flow is investigated. Flow properties in the presence of dual and triple shocks, generated through multiple arrays, resulting in parallel and coalescing configuration are characterized in some detail. The microjet-generated oblique shocks are reminiscent of the shocks generated by physical ramps (Fig. 1). A brief comparison of the microjet-shock with a physical ramp shock is also presented in the current study. Furthermore, such 'tailored shocks' generated using microjet arrays can possibly be implemented to decelerate the incoming flow in conjunction with a physical ramp and achieve better performance for inlets.

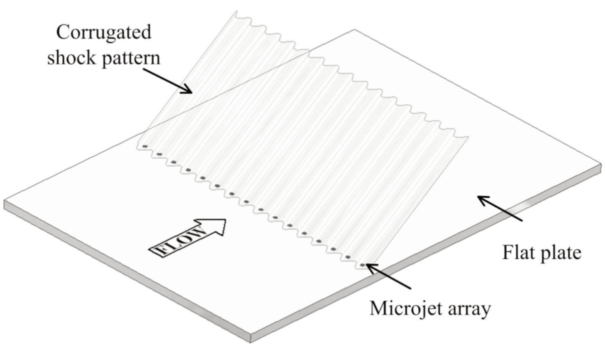

Figure 1. Schematic of the corrugated shock pattern with a microjet array.

2. EXPERIMENTAL DETAILS

2.1. Facility Description

The experiments are conducted in the supersonic wind tunnel facility at the Florida Center of Advanced Aero-Propulsion (FCAAP) at Florida State University (Fig. 2). The tunnel is supplied with dry, pressurized air from a 10 m^3 air tank at 11 MPa (1600 psi) Control of air flow to the test section is maintained through the use of two inline valves, a tescom dome regulator, and a Fisher control valve. The dome- loading regulator is used for the larger drop in pressure from the air tanks. An output pressure of 2.06 MPa (300 psi) from the dome regulator is maintained. The Fisher control valve is used for the fine control of the tunnel stagnation pressure and is operated via a PC-based LabVIEW data acquisition program. Two inline heaters with a combined power of 300 kW, capable of heating the air to 700 K (800 $^{\circ}$F), are installed to raise the stagnation temperature of the incoming air and to prevent condensation in the test section. The test section Mach number can be varied with the use of interchangeable nozzle blocks. Current experiments were performed at a test section Mach number of 1.5. The run time of the tunnel at these conditions is 10 minutes. The test section is 305 mm (12 in) long, 66 mm (2.6 in) wide and 44 mm (1.73 in) high with optical access from the sides and bottom. The stagnation pressure and temperature were typically maintained at 193 kPa (28 psi) and 330 K (135 $^{\circ}$F), respectively. A LabVIEW based data acquisition program was used to measure and record the run conditions, as well as control the wind tunnel.

2.2. Model Details and Test Conditions

The model used for the current experiments is a flat plate with microjet arrays located at four different locations along the length of the model. The model spanned the length and width of the test section. The location of the first microjet array A1 is 50 mm (1.1H) from the leading edge of the model. Subsequent microjet arrays A2, A3, and A4 are spaced evenly at 15 mm (x/H = 0.34, where H = 44 mm is the test section height) downstream of preceding array. A schematic of the flat plate model showing the flow direction, microjet array locations, axes origin, and the spacing between the arrays is shown in Fig. 3(a). The microjet arrays spanned the width of the model having an orifice diameter of 400 μm and are spaced

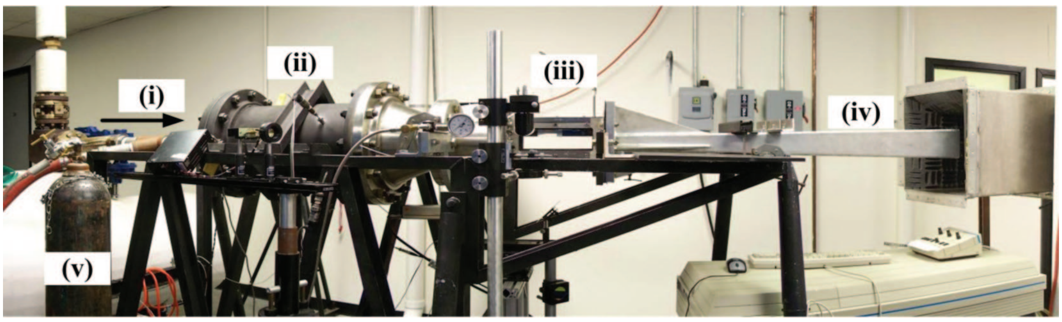

Figure 2. Layout of the supersonic wind tunnel (i) Air supply, (ii) Settling Chamber, (iii) Test Section, (iv) Diffuser, (v) Nitrogen supply for microjets.

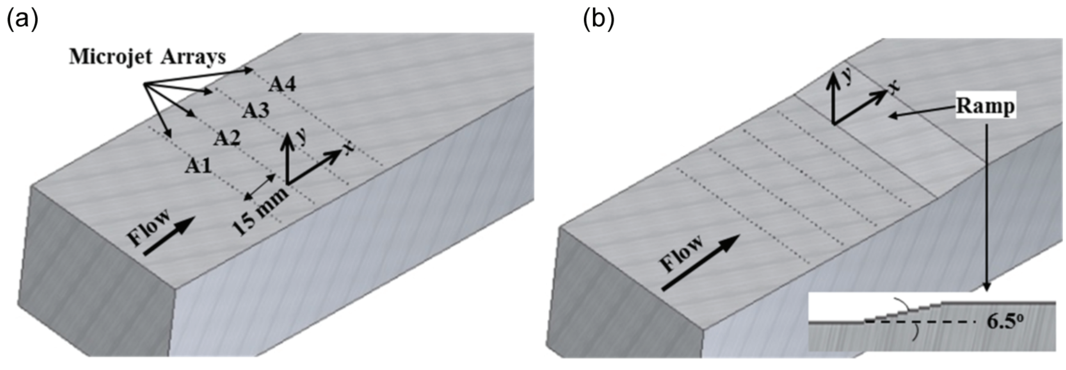

Figure 3. (a) Left: Schematic of the flat plate model showing the four microjet arrays A1–A4 and (b) Right: Schematic of the model with a 6.5° compression ramp.

evenly at 2 mm with a total of 31 microjets in one array. Each microjet array had their own stagnation chamber and supply line so that the momentum of the jets exiting is uniform. Pressurized gas from a nitrogen cylinder is routed to the microjet arrays via a manifold. Needle valves are used for fine control of the pressure supplied to the microjet arrays, and a resolution of ±1 psi was realized and maintained. The stagnation pressure of the microjet arrays is measured using Omega PX303-200G5V transducers. The stagnation pressure of the microjets is controlled to generate oblique shocks of desired strength. The flat plate is modified and a 2-D ramp that is 2.54 mm (0.1 in) high and spans the width of the model (66 mm) with a ramp angle of 6.5° is mounted on the model. The length of the compression surface of the ramp is one-half the height of the test section. A schematic of the ramp mounted on the flat plate is shown in Fig. 3(b). The origin of the coordinate system is at the microjet array A2 for the flat plate model and at the ramp corner for the compression ramp model as shown in Fig. 3.

The tunnel static and stagnation pressures were monitored using an Omega PX303-015A5V and PX205-100GI pressure transducers respectively. The ratio of the tunnel static and stagnation conditions is used to establish the desired Mach number. The microjet supply pressure was measured using an Omega PX303-200G5V, and is used in the calculations of MPR, where MPR is defined as the ratio of total microjet supply pressure and the tunnel stagnation pressure.

$$MPR = \frac{P_{o,\, microjet}}{P_{o,\, tunnel}} \tag{1}$$

2.3. Experimental Techniques

A conventional Z-type toepler schlieren arrangement with two parabolic mirrors and two flat mirrors is used for shadowgraph flow visualization. The white-light source used is a pulsed, Xenon flash lamp with a frequency up to 1000 Hz, and pulse duration of 5–10 μs.

Velocity field measurements along the centerline of the model are carried out using Particle Image Velocimetry (PIV). A dual cavity Spectra Physics PIV 400 Nd-YAG laser with a maximum power output of 300 mJ/pulse and a repetition rate of 15 Hz is used to illuminate the seed particles in the flow field. The flow is seeded with submicron size particles generated by a modified Wright nebulizer (details are given in Alkislar (2001)) that uses a water base and glycol solution (Rosco fog fluid). The particles are introduced into the flow upstream of the settling chamber to facilitate mixing of the seed with the flow.

The influence of the microjet and ramp generated shocks on the global flow field is investigated using a field of view of 58 mm (1.2H) × 44 mm (H). The images are recorded using an Imager pro X2M camera having a resolution of 1600(h) × 1200(v) and processed using DaVis 7.2 software. A typical dataset of 1200 instantaneous PIV image pairs are used to compute the velocity field statistics. For the acquiring the global flow field, a pulse separation of 1.5 μs is used which corresponds to a displacement of 11 pixels in the freestream. The zoomed in data presented in §3.2.1 (12 mm × 9 mm) for the microjet-generated shock is acquired with a pulse separation of 0.7 μs which corresponds to a dynamic range of 35 pixels in the freestream. An interrogation window of 32 × 32 pixels with a 50% overlap is used for all the cases. The obtained velocities are normalized by the isentropic velocity (U_o = 450 m/s), and the typical scale used for normalizing the length is the test section height H = 44 mm.

2.4. Measurement Uncertainties

The pressure data for the tunnel static, stagnation and microjet supply is sampled at a 1000 Hz using a National Instruments PCI-MIO-16E, 12 bit data acquisition card. The uncertainties in the measurement of the tunnel static and stagnation pressure are ± 0.2 kPa (0.04 psi) and ± 1.7 kPa (0.25 psi) respectively. The ratio of the tunnel static and stagnation pressure is used to calculate the Mach number with an uncertainty of 1%. The microjet supply pressure is estimated to have an error of ± 3.4 kPa (0.5 psi).

For the PIV measurements it is estimated that 90% of the particles introduced into the incoming flow were less than 0.5 μm with a nominal diameter of 0.3 μm (Alkislar [20]). The microjets in the present study were not seeded. The size of the particles determines the ability of the particles to track the flow gradients. The particle relaxation time τ_p, is calculated using the modified Stokes law based on the method suggested by Melling [21]. For a particle diameter d_p of 0.5 μm and density ρ_p of 1.2×10^3 kg/m^3, the particle relaxation time is found to be 1.04 μs. The choice of characteristic length scale for the current study is based on the maximum gradient that the flow undergoes. Since microjet arrays are used to generate oblique shocks, the maximum gradient of interest that the flow underwent is the drop in velocity across the strongest microjet-generated oblique shock (MPR = 4.1) tested here. The distance between the points where the flow velocity drops from the freestream to a minimum value behind the microjet-generated oblique shock, is used as the characteristic length scale and is found to be x/H = 0.1 (4.4 mm). The characteristic flow time scale τ_f was then calculated as 9.7 μs based on the freestream velocity of 450 m/s. The Stokes number (the ratio particle relaxation time to the characteristic flow time scale) and is found to be 0.11 approximately, therefore the particles are expected to track the velocity to within 2% of the flow velocity (Samimy and Lele [22]).

3. RESULTS AND DISCUSSION

The microjet array is operated at various supply pressures. For the present study the metric of choice was the microjet pressure ratio (MPR) defined by equation 1. Some of the other metrics often used in the literature on jets in crossflow include the momentum flux ratio (J) and the momentum coefficient (C_μ). Table 1 summarizes the run conditions of the microjet array. The amount of the mass utilized by the microjet array (m_{MJ}) is also presented as the ratio of the microjet array mass to the tunnel (m_{tunnel}) and boundary layer mass (m_{BL}).

$$J = \frac{\left(\gamma p M^2\right)_{MJ}}{\gamma p M^2_{\;tunnel}} \tag{2}$$

$$C_\mu = \frac{Blown\ mass\ ratio \times Jet\ velocity}{Dynamic\ pressure \times Area\left(BL\ thickness \cdot width\right)} = \frac{\left(no.\ of\ jets\right)\times\left(\gamma p A M^2\right)}{\left(0.5\gamma p M^2\right)_{tunnel}\times\left(\delta_{BL}\cdot w\right)} \tag{3}$$

3.1. Baseline Flow

A shadowgraph image showing the baseline conditions for the incoming flow is presented in Fig. 4(a). The image shows the location of microjet array A2 and the Mach waves emanating from the surface joints. The incoming velocity shown in Fig. 4(b) has a top hat profile measured at the location of microjet array A2. The difference between the top and bottom of the profile is due to the change in the surface geometry due to the presence of microjet arrays on the top wall of the test section (y/H = 0). The incoming boundary layer thickness is estimated from the velocity profile to be 4 mm (0.1H), approximately. In the following, the results of the single microjet-generated shock at MPR = 4.1 and a

Table 1. Operating conditions of the microjet array

$P_{o,MJ}$ (psia)	MPR	m_{MJ} (kg/s)	J	C_μ	m_{MJ}/m_{tunnel} (%)	m_{MJ}/m_{BL} (%)
29.7	1.1	0.002	0.9	0.03	0.2	2.1
39.7	1.4	0.003	1.2	0.04	0.3	2.8
64.7	2.3	0.004	2.0	0.06	0.4	4.6
89.7	3.2	0.006	2.8	0.08	0.6	6.4
114.7	4.1	0.008	3.5	0.10	0.8	8.2

(a)

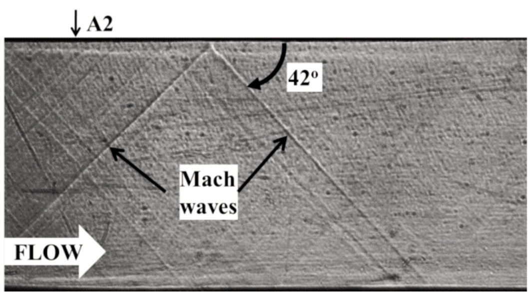

(b)

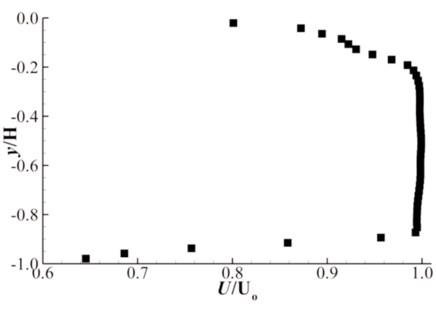

Figure 4. Baseline flow conditions (a) Left: Shadowgraph image (b) Right: Incoming velocity profile.

6.5° ramp shock will first be presented in the form of flow visualization using shadowgraph. Velocity field data and quantitative comparison of the microjet-generated shock and ramp shock on the flow field will then be discussed. This will be followed by a comparison of shadowgraph, Background Oriented Schlieren (BOS) and PIV results for a single microjet shock. A subsequent discussion of the parallel and coalescing shocks flow field is presented following the single array results.

3.2. Flow Visualization of Microjet-generated Shock at MPR = 4.1

The shadowgraph image in Fig. 5(a) shows the basic features of the shock generated by a single microjet array. The acronyms in Fig. 5 are used in our discussion. The reader is reminded that the actuator arrays are on the test section ceiling for this study. As the jet issues into the supersonic crossflow, it is rapidly turned in the downstream direction forming an incident oblique (IS) shock, which is a typical phenomenon in such flow fields (Kumar et al. [19]). Since the microjets issuing are highly underexpanded, the expanding jet core is seen as dark region near the jet exit (marked by arrow A2). The angle of the incident oblique shock is calculated to be 51.6°. The microjet-generated oblique shock was followed by an expansion fan (EF) that is immediately downstream of the injection location. The incident shock (IS) reflects from the lower tunnel wall and the reflected shock (RS) is inclined at 47.7°. The expansion fan that originates downstream of the injection location interacts with the reflected shock. The incident oblique shock undergoes an irregular Mach reflection (IR) forming the well-known normal shock or Mach stem at the bottom wall of the test section. The interaction of the incident shock with the boundary layer causes a pressure rise, that tends to propagate upstream in the subsonic region of the boundary layer causing the boundary layer to thicken both upstream and downstream of the interaction, as seen in the lower boundary layer in Fig. 5(a). The equivalent flow deflection angle termed as virtual deflection angle is calculated based on the incoming Mach number (1.5) and the microjet-generated incident oblique shock angle (51.6°) and is found to be approximately 6.5°.

The principal features of the interaction of the microjet-generated shock with the incoming crossflow as observed from the shadowgraph images are summarized in the flow field schematic shown in Fig. 5(b). The schematic helps in analysis of the shadowgraph images as well as correlating the flow visualization data with the velocity field data (discussed later). Typical features such as the λ–shock structure near the jet exit, expanding jet core, incident shock (IS), reflected shock (RS), expansion fan (EF) are shown the in the schematic. The interaction of the expansion fan with the reflected shock is also depicted in the schematic, which becomes clearer in the discussion of the velocity field results in the subsequent sections.

3.3. Velocity Field Microjet-generated Shock at MPR = 4.1

The mean streamwise (U/U_o) and cross-stream (V/U_o) velocity contours for the shock generated by the microjet array A2 (see Fig. 3(a)) operating at MPR = 4.1 are shown in Fig. 7(a–b). The axes are defined such that the location of the microjet array A2 is at the origin $x/H = 0$, where H is the test section height (44 mm). The location of the microjet arrays has been marked in each contour plot for clarity. Velocity data very close to the wall (near the microjet array) is corrupted due to unavoidable reflections of the

(a) (b)

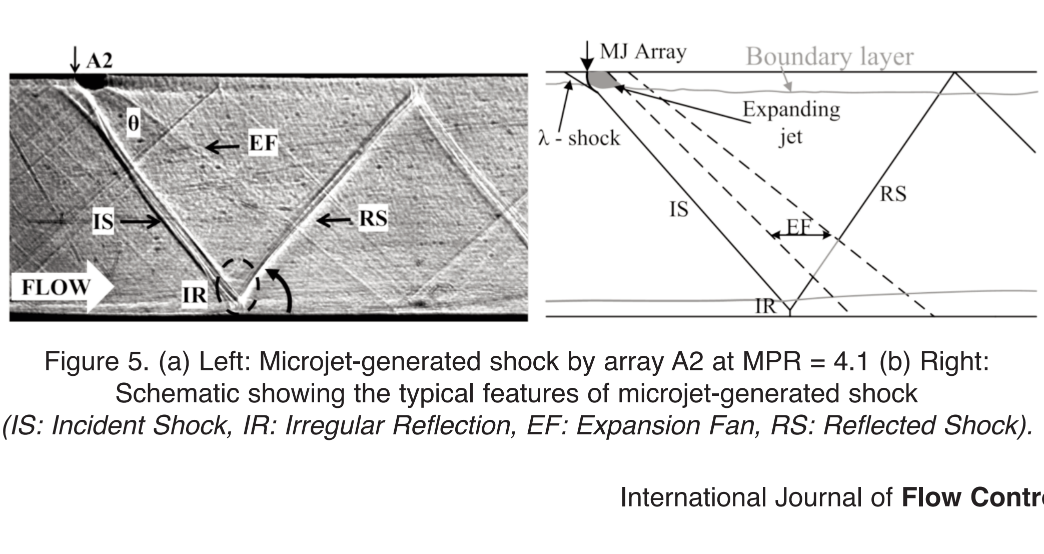

Figure 5. (a) Left: Microjet-generated shock by array A2 at MPR = 4.1 (b) Right: Schematic showing the typical features of microjet-generated shock
(IS: Incident Shock, IR: Irregular Reflection, EF: Expansion Fan, RS: Reflected Shock).

laser sheet from the flat plate model, and is not shown here. The microjet-generated shock is relatively weak which leads to a rather small gradient in the streamwise velocity across the shock. Thus, the levels in streamwise velocity contours in Fig. 7(a) have been adjusted to clearly show the drop in the velocity across the microjet-generated incident oblique shock and other relevant features such as the expansion fan and the reflected shock.

The global features observed in the velocity field measurements are similar to those in the shadowgraph image (Fig. 5) as expected, however significantly more detail, and quantitative information can be extracted from the velocity field. Near the exit of the micro-orifices the U/U_o contours have values of 0.8 (shown by black line) that shows the jet penetration into the freestream. As the jet penetrates further into the freestream, typical values of 0.91 for U/U_o are observed. The regions of low velocity are in part due to turning of the freestream due to the formation of the oblique shock upstream of the jet, and not entirely due to the penetration of the jet into the freestream. The presence of the incident oblique shock is marked by the U/U_o contour line of 0.99 (solid grey line in Fig. 6(a)), which is the first indication of flow turning. Since the microjet-generated shock forms a λ-shock structure that is unsteady in nature, an exact value of the upstream influence is difficult to find due to the smearing effect of the shock as a result of ensemble averaging. The increased width of the shock is also partly attributed to the particle lag associated with the PIV measurements. Using a contour value of $U/U_o = 0.99$, the upstream influence of microjet-generated shock is estimated to be $x/H = -0.11$, approximately.

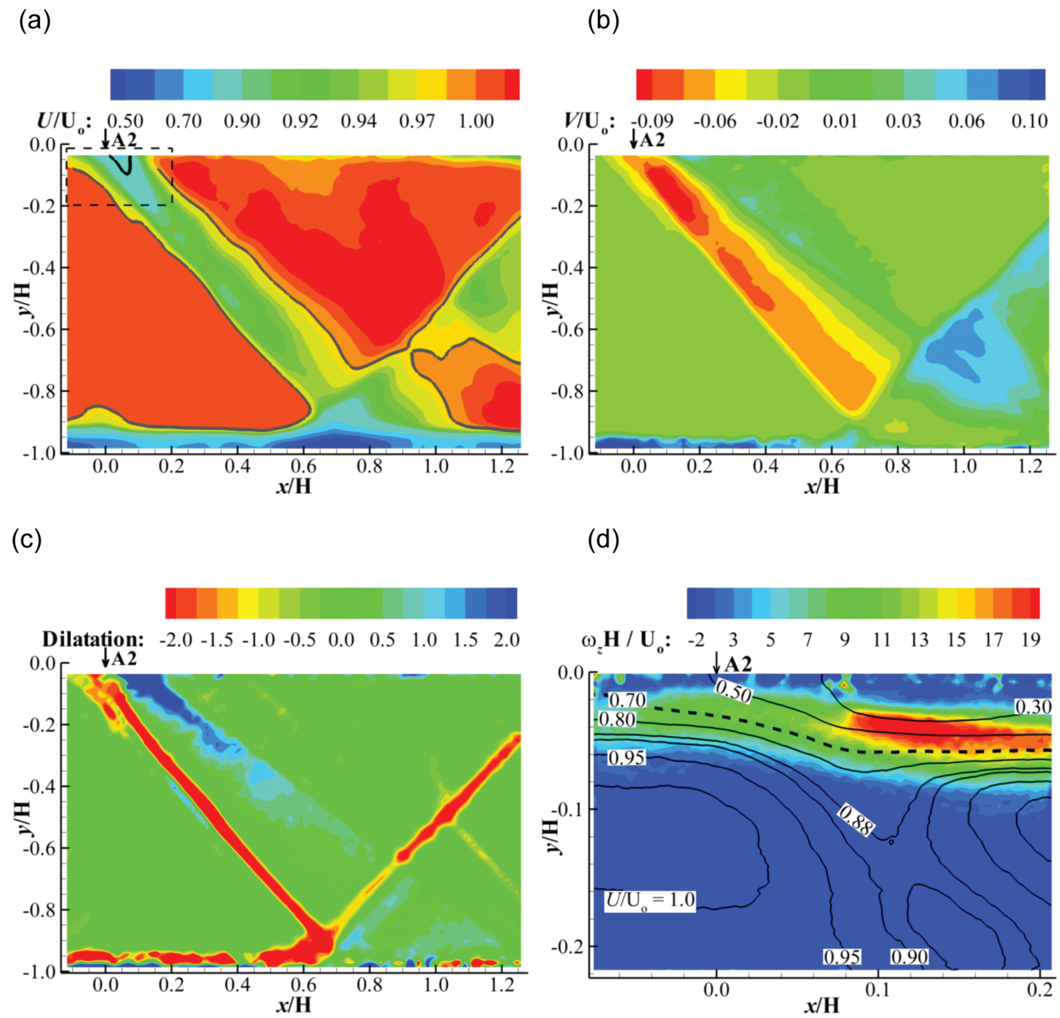

Figure 6. Velocity field for microjet-generated shock (a) U/U_o contours, (b) V/U_o contours, (c) Dilatation contours, and (d) Zoomed-in vorticity contour (refer to inset in (a)) (Flow: left to right).

Immediately downstream of the microjet-generated shock, region of flow acceleration resulting in streamwise velocities higher than the freestream is present, corresponding to an expansion fan. The expansion fan turns the flow parallel to the wall after the deflection through the incident oblique shock. The negative V/U_o values seen in Fig. 6(b) signify downward deflection of the flow through the incident shock wave, and positive values in the expansion fan and the reflected shock signify an upward deflection. An average cross-stream velocity of about $V/U_o = -0.07$, corresponding to yellow-red contours, is present near the center of the shock. The cross-stream velocity (V/U_o) contours show significant negative velocities with a magnitude of –0.09 near jet exit, and close to the edge of the boundary layer (0.1H), which is an indication of the strong penetration of the micro-jets into the crossflow. The significant penetration of the injectant into the freestream results in generating streamwise vorticity (see Alvi et al. [9]; Mahesh [4]; Fernandez et al. [23]) and leads to higher mixing with the freestream flow. This feature was exploited in another study where microjet arrays are used as mixing enhancement actuators upstream of a backward facing step in a supersonic flow (Ahmed et al. [24]).

Near the bottom wall, the incident oblique shock interacts with the incoming boundary layer, leading to regions of low velocity at the bottom wall where the magnitude of U/U_o reaches values as low as 0.5. This region can be clearly seen by the upward deflection of the contours near $x/H = 0.7$ in Fig. 6(a–b). The incident shock then reflects of the bottom wall through an irregular reflection where the reflected shock is weaker than the incident shock. The streamwise velocity level $U/U_o = 0.7$ (corresponding to M = 1) is used to approximately identify the triple point near the bottom wall. The triple point is found to be at $x/H = 0.7$ and $y/H = -0.91$, approximately. The streamwise velocity within the reflected shock ranges from 0.8 near the bottom wall to 0.96 in the center of the reflected shock, as seen in Fig. 6(a). The reflected shock interacts with the expansion fan emanating downstream of the injection location. The velocity levels(U/U_o) of the reflected shock increase to 0.98 in the vicinity of the interaction of the expansion fan with the reflected shock. Following the interaction, the velocity levels (U/U_o) of the reflected shock relax roughly to its original value of 0.96. These flow features are clearly depicted in the schematic shown in Fig. 5(b), and they have also been indicated in the dilatation contours in Fig. 6(c), discussed next. Here dilatation is defined as:

$$Dilatation = \frac{\partial(U/U_o)}{\partial(x/H)} + \frac{\partial(V/U_o)}{\partial(y/H)} \tag{4}$$

The dilatation contours help enhance certain features that are difficult to observe from the mean streamwise and cross-stream velocity data. For example, due to the smearing of the unsteady shock in the averaging process, the location of the shock is difficult to estimate from the mean velocity field. However, dilatation clearly shows the high velocity gradients present due to the shock in the flow field. The negative values of dilatation (red regions) denote compression by the shock wave, followed by positive values (blue regions) in the expansion fan of the flow field. The incident shock, reflected shock and the interaction of the reflected shock with the expansion fan are clearly observed in Fig. 6(c). As seen here and as expected, the compression of the flow by the shock wave occurs over a narrower region and the extent of compression is nearly constant along the extent of the shock.

To gain further insight into the interaction of the microjet-generated shock, a zoomed in PIV interrogation window (10 mm × 12 mm, see inset in Fig. 6(a)) is used. The vorticity contours superimposed with selected line contours of streamwise velocity are presented in Fig. 6(d). The zoomed-in contours show features seen in the global flow field contours, albeit in greater detail. The effect of injection is clearly seen by the downward deflection of the U/U_o contour lines. The occurrence of low velocity fluid ($U/U_o = 0.3$) in the immediate downstream vicinity of the microjet injection location in the crossflow is a flow feature that is observed when a single jet (typically much larger in diameter than the microjets) is injected in a crossflow (Papamoschou and Hubbard [2]). The occurrence of low velocity fluid region behind a jet in crossflow is a consequence of the formation of the barrel shock around the expanding jet core at the jet-crossflow boundary. The vorticity generated is primarily due to dilatation effects associated with the shock generated by the microjets. The high vorticity regions (red contours) lie below the sonic line ($U/U_o = 0.7$) as shown in the figure. Due to jet injection the exact extent of the perturbed boundary layer is difficult to identify. Thus, the $U/U_o = 0.95$ line is defined as the edge of the shear layer. The bulk of the vorticity generated lies within the shear layer as seen from Fig. 6(d).

The vorticity generation proves the enhanced mixing capability of the microjet based actuators that has been experimentally investigated in supersonic cavity (Zhuang et al. [8]) and backward facing step (Ahmed et al. [24]) flow.

The shock angles are computed from the mean streamwise velocity contours. The velocity gradient across the shock wave is used to identify the location of the approximate shock center. The slope from the linear fit of the shock center locations is used to calculate the oblique shock angles. The incident oblique shock angle is calculated to be 51.4°. The reflected shock angle is calculated and found to be 47.9°. The angles calculated from velocity field data are found to be in very good agreement with the angles from the shadowgraph images, providing further confidence in both measurements and the conclusions drawn from therein.

3.4. Effect of Microjet-generated Shock on the Flow Field

The velocity profile at the test section centerline (y/H = –0.5) = showing the incident shock, expansion fan, and the reflected shock at MPR = 4.1 is shown in Fig. 7(a). The profile is obtained by extracting data at y/H = –0.5 from the streamwise velocity contour shown in Fig. 7(a). The velocity drop across the incident shock is calculated as $U/U_o = 0.9$, which is larger than the velocity drop across the reflected shock. The result is expected as the reflected shock angle (47.9°) is less than the incident shock angle (51.4°), and the flow upstream of the reflected shock has been decelerated. The plot highlights the typical features in the flow field. The incoming free stream flow is compressed by the incident oblique shock. The flow then recovers through an expansion fan that originates immediately downstream of the incident oblique shock as seen in the shadowgraph images (Fig. 5), velocity, and dilatation contours. The flow undergoes a second compression that is milder than the initial compression by the reflected shock wave before straightening out. These features, their approximate locations and regions of influence are indicated in Fig. 7(a).

The extent of influence of the microjet-generated shock and expansion fan on the flow field is shown in Fig. 7(b). The profile representing the incident shock (square symbols) represents the location of the maximum gradient of U/U_o across the shock. The expansion fan curve (diamond symbols) is obtained by finding the location where the cross-stream velocity (V/U_o) is zero, which corresponds to straightening of the flow by the expansion fan following the initial turning due to the incident shock wave. The plot helps in highlighting shock and expansion fan inclination along the test section height. Similar discussion about the expansion fan was presented earlier using the dilatation contours in Fig. 6(c). The above plot shows that the expansion fan after the first microjet shock can affect the shock generated by a second microjet array, if the second microjet array lies within x/H = 0.45 (x = 19 mm). This result is significant when using multiple microjet arrays along the surface (see Fig. 3(a)), to generate multiple parallel, and/or coalescing shocks, as discussed in sections to follow.

The strength of the microjet-generated shock as it propagates across the test section is investigated by examining the velocity change across the shock. Streamwise velocity distribution at various locations (y/H) across the test section height is analyzed. The schematic shown in Figure 8(a) shows some of the extraction locations. The origin of the coordinate system is x_o, which is also the location of the microjet array (A2), as marked in the figure. For ease of interpretation, and to provide a more

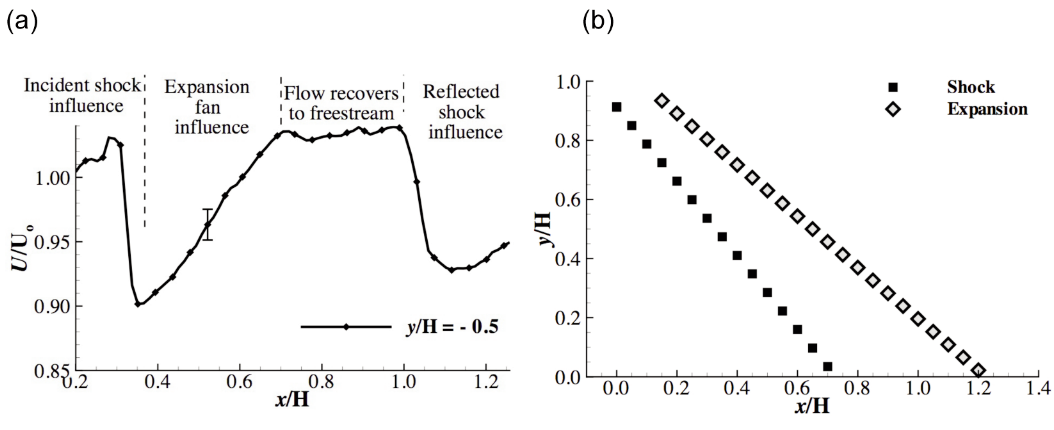

Figure 7. Effect of microjet-generated shock (a) Streamwise velocity profile at the test section centerline (y/H = –0.5) and (b) Influence of the shock and expansion fan.

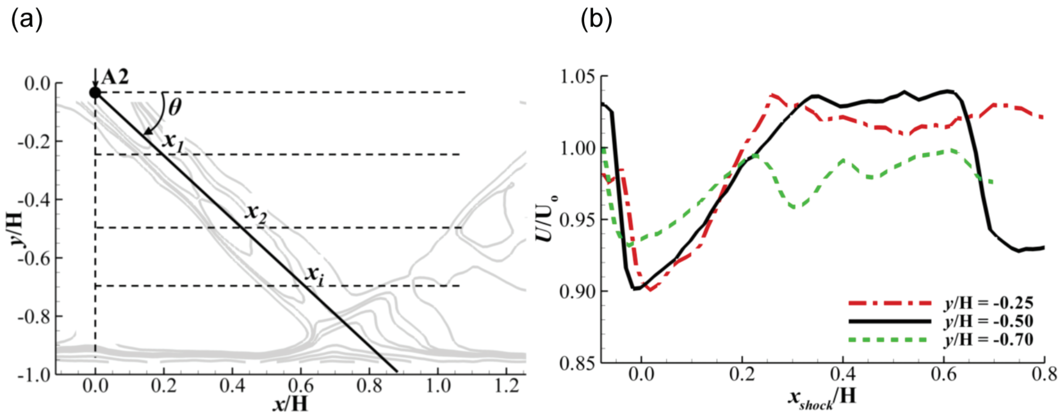

Figure 8. (a) Left: Schematic showing the streamwise velocity profile extraction locations and (b) Right: Velocity profiles.

physical perspective, a simple coordinate transformation was carried out such that the velocity profiles collapse on top of one another. The distance of the center of the shock from the origin x_o is defined as x_{shock}/H where,

$$x_{shock}/\mathrm{H} = (x_i - x_o)/\mathrm{H} \tag{5}$$

The location at any height x_i is then calculated as,

$$x_i = (y/\mathrm{H})/\tan\theta \tag{6}$$

and θ is the oblique shock angle found to be 51.4° for the microjet-generated shock from the PIV data.

The velocity distributions at y/H = –0.25, –0.50, and –0.70 are shown in Fig. 8(b). Additional profiles along the test section height were also examined but are not shown to avoid clutter. The profiles near the top and bottom wall of the test section are not used to exclude the effect of the wall boundary layer on the inviscid portion of the shock. The values of $U/\mathrm{U_o}$ range from 0.90 ± 0.02 at y/H = –0.25 to 0.93 ± 0.02 at y/H = –0.70. In the middle/inviscid part of the shock, typical values of $U/\mathrm{U_o}$ ~ 0.90 are seen from the profile. The velocity distributions in Fig. 8(b) show that the strength of the shock in terms of the velocity drop varies being stronger near the microjet injection location, and weaker as one moves away from the point of injection location, and approaches the bottom wall. This observation confirms that, in the limit of increasing y/H, the shock wave will eventually relax to a Mach wave. The influence of the microjet shock on the velocity field spreads across x_{shock} = 0.3H (13 mm) approximately in the downstream streamwise direction, with an average change in velocity being $U/\mathrm{U_o}$ = 0.91. At x_{shock}/H = 0.3, a second drop in the velocity profile is also observed due to the presence of the reflected shock.

3.5. Effect of MPR on Single Microjet-generated Shock

The effect of MPR on the shock strength is discussed in terms of velocity change ($U/\mathrm{U_o}$). The velocity distributions along the streamwise direction are presented in Fig. 9(a–c) for varying MPR. The figure

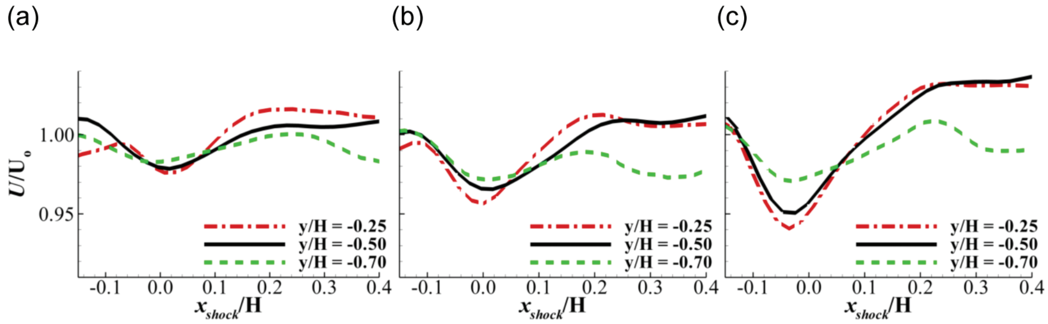

Figure 9. Shock strength in terms of mean streamwise velocity at various y/H locations (a) = MPR 1.4, (b) MPR = 2.3, and (c) MPR = 3.2.

shows the velocity profiles at three different test section locations, y/H = –0.25, –0.50, and –0.75. The error bars showing the uncertainty in velocity are also shown. The streamwise coordinate has been scaled to x_{shock}/H to collapse the profiles on top of one another and to aid the comparison. The shock strength increases with increasing MPR and is reflected in the velocity drop across the shock. For low values of MPR = 1.4, the shock generated is weak causing a very small change in the velocity across it. For slightly higher values of MPR = 2.3, the velocity change across the shock increases as seen in Fig. 9(b). At MPR = 3.2, the shock becomes stronger with a velocity change of U/U$_o$ = 0.94.

3.6 Multiple Microjet-generated Shocks

3.6.1. Parallel Shocks

The capability of generating nearly parallel oblique shocks by using two or three microjet arrays operating simultaneously at the same MPR has been demonstrated previously (Kumar et al. [19]). In the earlier study, two parallel shocks were generated using microjet arrays A2 and A3 operating at the same MPR = 1.1. The oblique shock angles for the two parallel shocks were found to be 45.2° and 44.8° for arrays A2 and A3, respectively. In this study, the approach is extended to three parallel shocks using microjet arrays A2, A3, and A4 operating at MPR = 1.1. We note that, only relatively low MPR values could be tested as higher microjet pressure result in stronger shocks and strong multiple shocks led to tunnel unstart. The shadowgraph image in Fig. 10(a) shows three parallel shock and expansion fan system generated by using microjet arrays A2, A3, and A4. The angles measured from the shadowgraph image for shocks generated by arrays A2, A3, and A4 are 44.1°, 44.1°, and 44.5°, respectively.

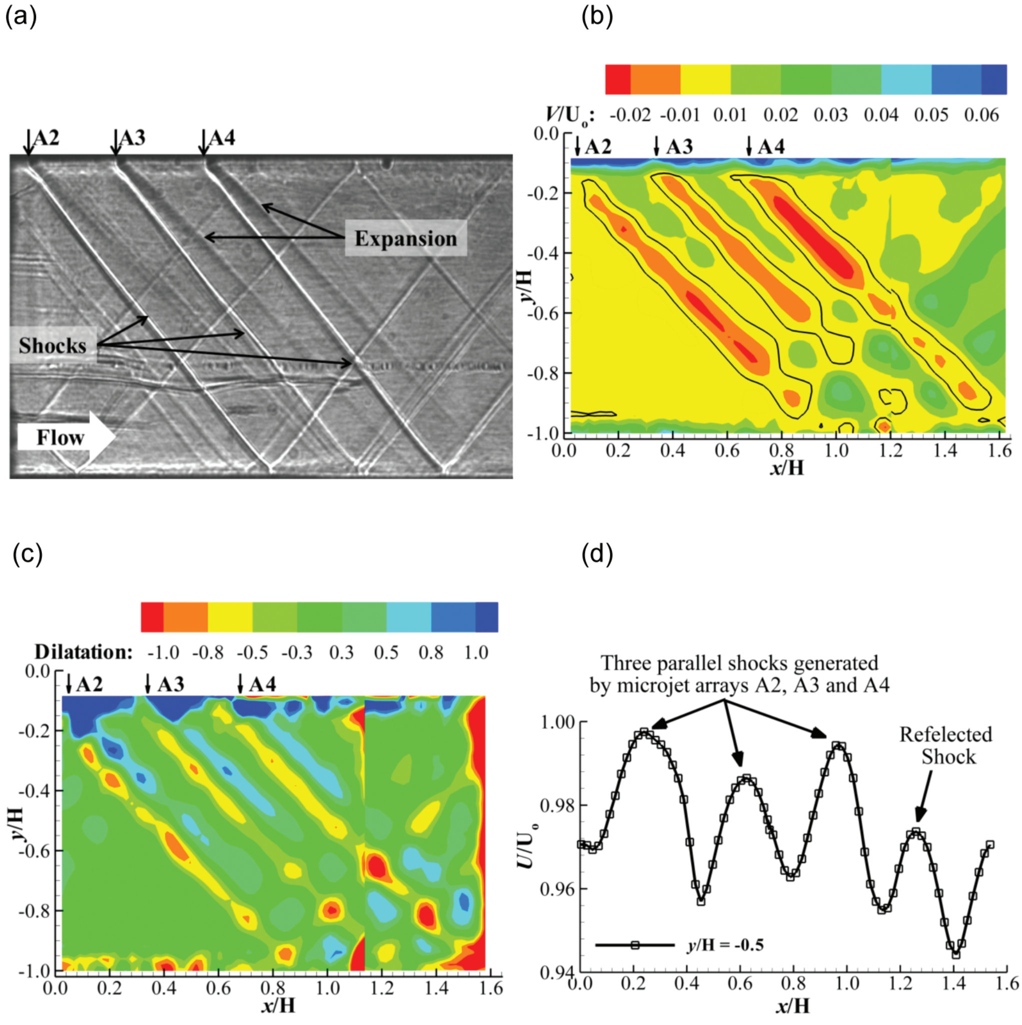

Figure 10. Velocity field of parallel shocks at MPR = 1.1 (a) shadowgraph image, (b) mean cross-stream velocity, (c) dilatation, and (d) U/U$_o$ distribution along the streamwise direction at the test section centerline (y/H = –0.5).

The effect of multiple shocks on the flow field is investigated by analyzing the velocity field. The origin (x/H = 0) of the coordinate system is set at the location of microjet array A2. Subsequent arrays A3 and A4 are referenced relative to array A2 and are evenly spaced at Δx/H = 0.34. Two PIV imaging windows are used to capture the entire flow field with the three parallel shocks. The overlap between the two windows can be seen in Fig. 10(b–d) as a discontinuity in the contours. It is shown in the previous sections that the strength of the shock increases with increasing MPR. Thus, the shocks generated at MPR = 1.1 are weaker than the single shock case discussed earlier, making the effect of these shocks on the mean streamwise velocity (U/U_o) rather difficult to analyze. However, the cross-stream velocity contours are more sensitive and are therefore more effective in showing the effect of multiple shocks on the flow field; these are shown in Fig. 10(b). The solid black lines represent the $V/U_o = 0$, that serves to identify the three shocks. Typical flow deflection in terms of the cross- stream velocity is $V/U_o = -0.01$ (orange regions in Fig. 10(b)). The expansion fans follow the microjet-generated shocks and are shown by the green regions between the three oblique shocks. The angle of the three shocks are computed from the velocity data, and are found to be 44.7°, 44.3°, and 44.9° for shocks generated by A2, A3, and A4 respectively. The angles from the shadowgraph and the velocity data complement each other. The dilatation contours in Fig. 10(c) further highlight the compression (yellow-orange regions) and expansion (blue regions) of the flow by the shock and expansion fan. The dilatation contour levels also show relatively weak gradients across the shock and expansion fan. Typical values of –0.8 and 0.8 are found in the compression and expansion regions, respectively. For the case presented here, it is observed that the effect of the expansion fan after the first shock does not influence the behavior of the second shock; similar behavior is seen by the expansion following the second shock and the interaction with the third shock. However, as the shock strength increases, the associated expansion fan will become stronger (as noted in the discussion of Fig. 9) and affect the second and third shocks. This behavior is discussed further by analyzing two shocks in sections to follow.

The influence of the multiple shocks on the flow field is seen from the streamwise velocity distribution at the test section centerline (y/H = –0 5) presented in Fig. 10(d). The presence of the three shocks is marked in the figure. The incoming flow is compressed by the first shock, the effect of which is seen between x/H = 0.24–0.45. The flow then recovers through the first expansion fan which spans over x/H = 0.45–0.61. The effect of the second shock ranges between x/H = 0.61–0.78, followed by an expansion that extends until x/H = 0.97. The effect of the third shock starts at x/H = 0.97 and lasts till about x/H = 1.13. The velocity change across the three shocks is U/U_o = 0.95, 0.96, and 0.95, respectively, which is within the uncertainty in the velocity measured by PIV. The reflected shock is also seen clearly from the velocity distribution, the strength of which is lower than the incident shocks.

3.6.2. Coalescing Shocks

The supply pressure (MPR) to the microjet arrays can be tailored to vary the oblique shock angles. Using two microjet arrays A2 and A3, parallel and/or coalescing shocks can be generated. By adjusting the pressure ratios, these two shocks can be systematically tailored to coalesce at the bottom wall of the test section and reflect as a single shock, thereby simulating the shock on lip conditions. By fixing the supply of the array A2 at MPR = 1.1, and gradually increasing the MPR of array A3, the shock generated by array A3 coalesced with the array A2 shock at the bottom wall of the test section. Figure 11 shows shadowgraph images of the intermediate asymmetric and coalescing cases. In the intermediate asymmetric case, the MPR of array A2 is 1.1, and A3 is 4.8. The image in Fig. 11(a) shows the two shocks from arrays A2 and A3 close to each other at the bottom wall (marked by the ellipse) and reflecting as two independent shocks. As the MPR of array A3 is increased to 5.8 (keeping A2 at 1.1), the two shocks coalesce at the bottom wall and reflect as a single shock as shown in Fig. 11(b). The coalescing point (shown by the circle) and the reflected shock are clearly marked in the figure.

Quantitative measurements were carried out for two cases, the intermediate asymmetric case and the coalescing case. The velocity field of the coalescing case is presented in Fig. 12(a–b) in the form of mean cross-stream velocity and dilatation contours. The streamwise velocity contour is not shown here due to large difference between the strengths of shocks at MPR = 1.1 and 5.8, which makes it difficult to identify the weaker shock. The contour plots for the approaching case are not shown, as they are similar in features to the coalescing case. The cross-stream velocity (V/U_o) contour in Fig. 12(a) shows the milder compression of the flow across the first shock (green-yellow regions); followed by a very small region where the expansion fan occurs following the first shock.

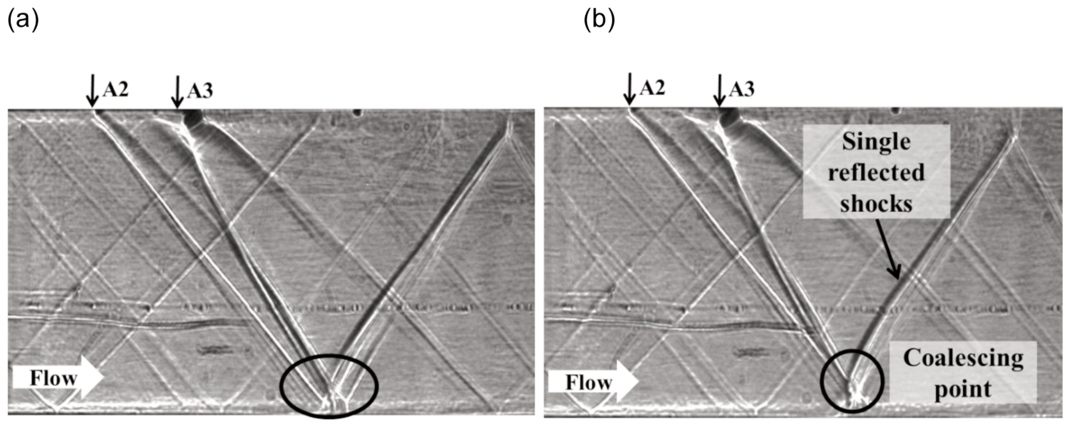

Figure 11. Shadowgraph images of two shocks generated by microjet arrays A2 and A3 (a) Intermediate asymmetric case and (b) Coalescing case.

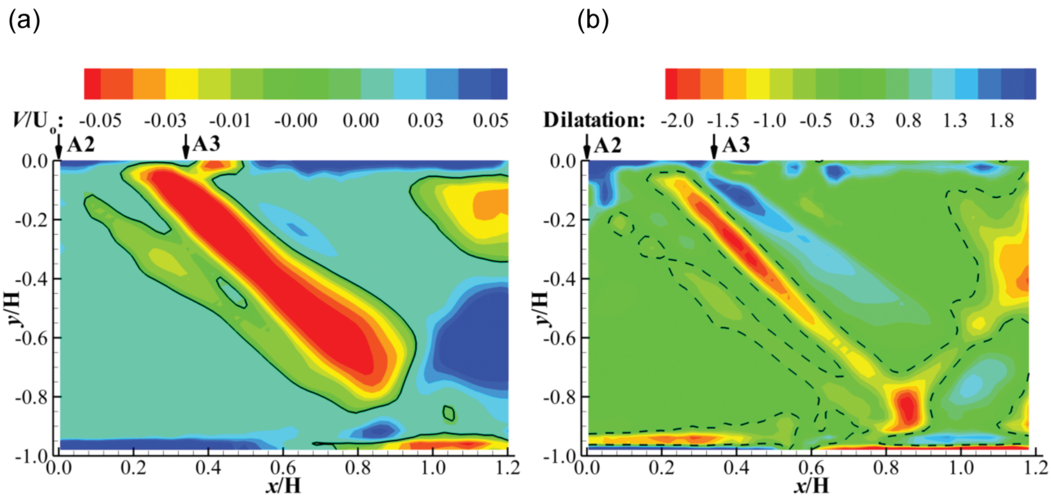

Figure 12. Contours of coalescing shocks generated by microjet arrays A2 and A3 operating at MPR = 1.1, and 5.8 respectively, (a) cross-stream velocity and (b) dilatation.

The second shock is much stronger (MPR = 5.8) as seen by the red regions in the contour plot with typical values of $V/U_o = -0.05$. The $V/U_o = 0$ is shown by a solid black contour line outlining the two shocks where the deflection of the flow occurs. The reflected shock is identified by the blue regions ($V/U_o = 0.05$) between x/H = 0.9 and 1.2. The two incident shocks and formation of one reflected shock is observed more clearly from the dilatation contours in Fig. 12b). The dashed line on the contour plot encompasses the location of the maximum gradients across the two shocks. This makes it easier to locate the shocks as compared to the cross-stream velocity contours. Typical dilatation values of –0.5 and –1.75 were found in the first and second shocks. The dilatation contour shows the presence of the expansion fan between the first and second shock wave. The contour also highlights the single reflected shock near x/H = 0.9.

The oblique shock angles for the intermediate asymmetric and coalescing cases are calculated for the two incident shocks and are tabulated in table 2. The strength of the shock is also quantified in terms

Table 2. Operating conditions for intermediate asymmetric and coalescing cases

	Array A2		Array 3	
	MPR	**Angle**	**MPR**	**Angle**
Intermediate asymmetric case	1.1	44.6°	4.8	49.1°
Coalescing case	1.1	45.2°	5.8	54.9°

of the velocity drop across the shocks. The streamwise velocity distribution along the test section centerline (y/H= –0.5) for the intermediate asymmetric and coalescing cases is shown in Fig. 13. For the intermediate asymmetric case the incoming flow is decelerated to $U/U_o = 0.96$.

The width of the expansion region ranges between x/H = 0.43 ~ 0.53. This is followed by the compression of the flow by the second shock to a value of $U/U_o = 0.92$ following which, the flow recovers to freestream conditions. For the coalescing case, the velocity drop across the first shock is the same as in the intermediate asymmetric case as in both cases microjet array A2 is operating at an MPR = 1.1. However, the expansion fan region is reduced and ranges between x/H = 0.43 and 0.49. This can also be seen from the shadowgraph images in Fig. 11(b) and the flow field contours in Fig. 12. The second shock further compresses the flow to a value of $U/U_o = 0.90$, before the flow recovers to freestream conditions. The results indicate that, within certain limits, a desired flow turning can be achieved by using a combination of multiple shocks (analogous to multiple ramps) to reduce some of the losses associated with the compression of flow through a single strong shock a desirable feature for supersonic inlet design.

3.7. Comparison with a Ramp

3.7.1. Flow Visualization

The shadowgraph image of a 6.5° 2-D compression ramp in a Mach 1.5 crossflow is presented in Fig. 14. Overall features similar to the microjet-generated oblique shocks seen in Fig. 5 are observed here – with some differences. The figure shows the incident shock (IS), reflected shock (RS) and expansion fan (EF). The incident oblique shock begins as a λ–shock system just upstream of the ramp corner. The incident shock undergoes an irregular reflection (IR) at the bottom wall of the test section. The choice of the ramp angle is dictated by the results obtained from the microjet-generated oblique shock at MPR = 4.1 discussed earlier. Based on the flow turning angle and the incoming Mach number, the flow deflection angle is calculated as 6.5°. Thus, the ramp angle is chosen to be 6.5°. The incident shock from the ramp is measured to be 51.9°. According to the 2-D oblique shock theory, the Mach number downstream of the incident shock for a flow deflection of 6.5° is 1.27. The required flow turning angle of 6.5° to bring the flow parallel to the bottom wall of the test section exceeds the maximum turning angle for this downstream Mach number, resulting in an irregular reflection at the bottom wall as seen in Fig. 14.

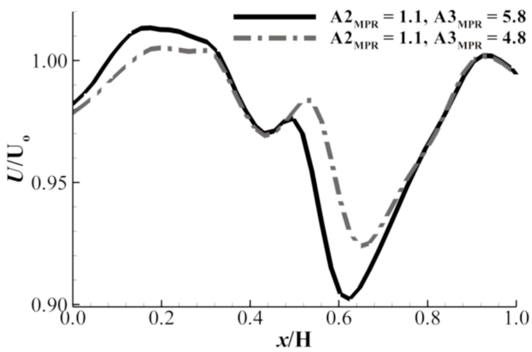

Figure 13. U/U_o distribution along the streamwise direction at the test section centerline (y/H = –0.5) for the intermediat e asymmetric and coalescing case.

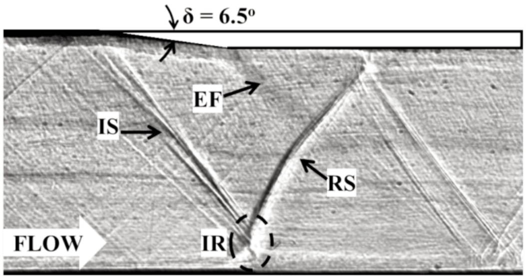

Figure 14. Flow over a compression ramp.

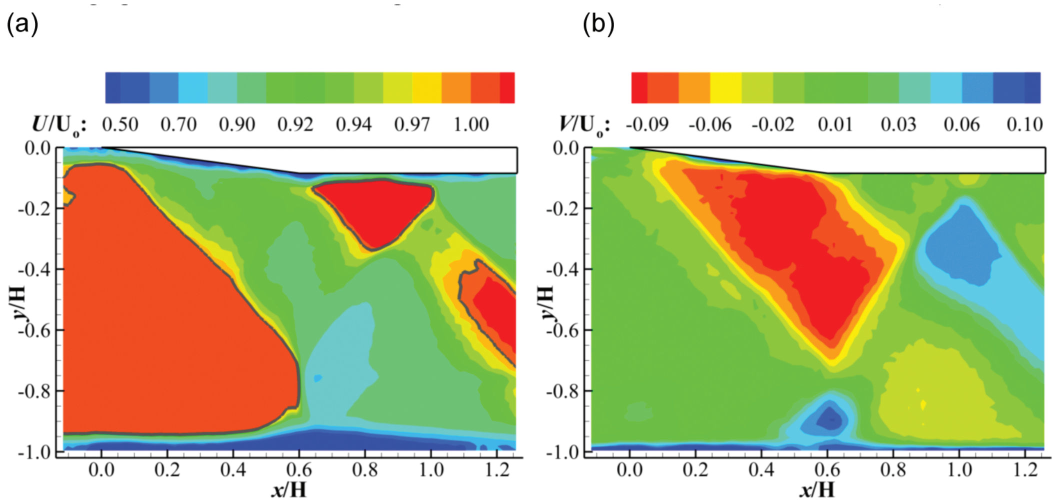

Figure 15. Velocity field data for a 6.5° 2-D compression ramp (a) U/U_o contours and (b) V/U_o contours (Flow: left to right).

3.7.2. Velocity Field Around a Compression Ramp

The mean streamwise and cross-stream velocity contours for the flow field around a 6.5° 2-D compression ramp are presented in Fig. 15(a–b). The axes are defined such that the location of the ramp corner is at the origin $x/\mathrm{H} = 0$. The incident oblique shock is marked by the U/U_o contour level (grey line) of 0.99 in Fig. 15(a), which is the first indication of flow deflection. This is followed by the compression of the flow along the ramp surface where typical values of U/U_o are 0.90. The incident shock being strong causes an irregular reflection at the bottom surface, which is also seen in the shadowgraph images. The presence of the Mach stem is also evident from the upward deflection of the streamwise velocity contours and thickening of the incoming boundary layer. The expansion fan emanates from the shoulder of the ramp turning the flow parallel to the freestream – this can be seen in Fig. 15(a) as the triangular region (red contours) originating near the ramp shoulder with velocities higher than the freestream. The compression of the flow is visualized clearly from contours of the cross-stream velocity (V/U_o) in Fig. 15(b) shown by the red contoursnegative values, as high as –0.09. The V/U_o contours also aid in the visualization of the weak compression waves that form the incident shock foot. These weak compression waves can be seen from the green-yellow contour levels in Fig. 15(b) (see Fig. 14, where the shadowgraph also reveals these compression waves at the foot of the incident shock, IS).

4. CONCLUSIONS

In this paper, both qualitative and quantitative measurements are obtained using flow visualization through shadowgraphs and velocity field measurements using PIV to study the characteristics of microjet-generated shocks. The effect on the flow field of the microjet-generated shocks is estimated in terms of the velocity drop across the shock. It was found that the strength of the shock remains nearly constant in the inviscid portion of the shock. The shock angle that is a measure of the shock strength increases with an increase in MPR for the range of tested conditions. The microjet-generated shocks produce significant amount of vorticity leading to enhanced mixing capability, which is desirable for certain applications such as fuel injectors in combustors. Multiple microjet-generated shocks were also examined. The flow field with three microjet-generated shocks at MPR = 1.1 showed that the shocks are of approximately equal strength and remained parallel to one another – an important design consideration for sonic boom mitigation problems. The influence of a first shock on the second shock is demonstrated by the intermediate asymmetric and coalescing cases. The presence of the first shock reduces the Mach number of the incoming flow before the second shock, thereby producing a higher shock angle for the same flow deflection. Thus, higher shock angles leading to stronger compression of the flow are achieved for the second shock in the presence of the first shock. A comparison of the microjet-generated shock at MPR = 4.1 with a shock generated by a 6.5° ramp showed that the microjet-generated shocks have some similarity to the ramp shock. It is noted that the microjet-generated shocks are capable of providing an equivalent turning of the flow as compared to a shock from a finite ramp. However, the spatial extent of the compression of the flow by the microjet-generated shock is smaller than the ramp shock. Future studies aim at employing the microjet-generated shocks in conjunction with a ramp to achieve improved compression of the flow: a result that would be useful for supersonic inlet problems.

ACKNOWLEDGEMENTS
This work was supported by Florida Center for Advanced Aero-Propulsion (FCAAP) at Florida State University. The authors would like to thank Robert Avant, the master machinist at FCAAP.

NOMENCLATURE

d	=	microjet orifice diameter, mm
M	=	Mach number
Mj	=	microjets
A1, A2, A3	=	microjet arrays
$P_{o,tunnel}$	=	tunnel stagnation pressure, kPa
$P_{o,microjet}$	=	microjet stagnation pressure, kPa
H	=	test section height, mm
MPR	=	Microjet Pressure Ratio
J	=	momentum flux ratio
C_μ	=	momentum coefficient
x/H	=	normalized streamwise coordinate
y/H	=	normalized cross-streamwise/wall-normal coordinate
U_o	=	freestream velocity, m/s
U/U_o	=	normalized streamwise velocity
$V U_o$	=	normalized cross-streamwise velocity

REFERENCES

[1] Gruber, M. R., Nejad, A. S., Chen, T. H., and Dutton, J. C., “Mixing and Penetration Studies of Sonic Jets in a Mach 2 Freestream,” *Journal of Propulsion and Power*, Vol. 11, No. 2, 1995, pp. 315–323.

[2] Papamoschou, D., and Hubbard, D. G., “Visual observations of supersonic transverse jets,” *Experiments in Fluids*, Vol. 14, 1993, pp. 468–476.

[3] Ben-Yakar, A., Mungal, M. G., and Hanson, R. K., “Time evolution and mixing characteristics of hydrogen and ethylene transverse jets in supersonic crossflows,” *Physics of Fluids*, Vol. 18, No. 2, 2006, p. 026101.

[4] Mahesh, K., “The Interaction of Jets with Crossflow,” *Annual Review of Fluid Mechanics*, Vol. 45, 2013, pp. 379–407.

[5] Ferry, A., “Mixing-Controlled Supersonic Combustion,” *Annual Review of Fluid Mechanics*, Vol. 5, No. 1, 1973, pp. 301–338.

[6] Seiner, J., Dash, S., and Kenzakowski, D., “Historical Survey on Enhanced Mixing in Scramjet Engines,” *Journal of Propulsion and Power*, Vol. 17, No. 6, 2001, pp. 1273–1286.

[7] Cattafesta III, L. N., Song, Q., Williams, D. R., Rowley, C. W., and Alvi, F. S., “Active control of flow-induced cavity oscillations,” *Progress in Aerospace Sciences*, Vol. 44, 2008, pp. 479–502.

[8] Zhuang, N., Alvi, F. S., Alkislar, M. B., and Shih, C., “Supersonic Cavity Flows and Their Control,” *AIAA Journal*, Vol. 44, No. 9, 2006, pp. 2118–2128.

[9] Alvi, F. S., Lou, H., Shih, C., and Kumar, R., “Experimental study of physical mechanisms in the control of supersonic impinging jets using microjets,” *Journal of Fluid Mechanics*, Vol. 613, 2008, pp. 55–83.

[10] Delery, J., and Marvin, J. G., “Shock-Wave Boundary Layer Interactions,” AGARDograph No. 280, 1986.

[11] Settles, G. S., and Dolling, D. S., “Swept Shock/Wave Boundary-Layer Interactions,” *Tacticle Missile Aerodynamics*, edited by M. Ilemsch and J. Nielsen, Vol. 104, Progress in Astronautics and Aeronautics, AIAA, New York, 1986, pp. 291–319.

[12] Viswanath, P. R., "Shock-wave-turbulent-boundary-layer interaction and its control: A survey of recent developments," *Sadhana*, Vol. 12, 1988, pp. 45–104.

[13] Settles, G. S., and Dolling, D. S., "Swept Shock/Boundary-Layer Interactions - Tutorial and Update," *AIAA Paper* 1990-0375, 1990.

[14] Dolling, D. S., "Fifty Years of Shock-Wave/Boundary-Layer Interaction Research: What Next?," *AIAA Journal*, Vol. 39, No. 8, 2001, pp. 1517–1531.

[15] Clemens, N. T., and Narayanaswamy, V., "Shock/Turbulent Boundary Layer Interactions: Review of Recent Work on Sources of Unsteadiness," *AIAA Paper* 2009-3710, 2009.

[16] Howe, D. C., Simmons III, F., and Freund, D., "Development of the Gulfstream Quiet Spike™ for Sonic Boom Minimization," *AIAA Paper* 2008-0124, 2008.

[17] Valdivia, A., Yuceil, K. B., Wagner, J. L., Clemens, N. T., and Dolling, D. S., "Active Control of Supersonic Inlet Unstart Using Vortex Generator Jets," *AIAA Paper* 2009-4022, 2009.

[18] Anderson, B. H., Mace, J. L., and Mani, M., "Active "Fail Safe" Micro-Array Flow Control For Advanced Embedded Propulsion Systems," *AIAA Paper* 2009-0741 2009.

[19] Kumar, R., Ali, M. Y., Alvi, F. S., and Venkatakrishnan, L., "Generation and Control of Oblique Shocks Using Microjets," *AIAA Journal*, Vol. 49, No. 12, 2011, pp. 2751–2759.

[20] Alkislar, M. B., "Flowfield Measurement in a Screeching Rectangular Jet," Ph.D. Thesis, Department of Mechanical Engineering, Florida State University, Fall, 2001.

[21] Melling, A., "Tracer particles and seeding for particle image velocimetry," *Measurement Science and Technology*, Vol. 8, 1997, pp. 1406–1416.

[22] Samimy, M., and Lele, S. K., "Motion of particles with inertia in a compressible free shear layer," *Physics of Fluids A: Fluid Dynamics*, Vol. 3, No. 8, 1991, pp. 1915–1923.

[23] Fernandez, E., Kumar, R., and Alvi, F., "Separation Control on a Low-Pressure Turbine Blade using Microjets," *Journal of Propulsion and Power*, Vol. 29, No. 4, 2013, pp. 867–881.

[24] Ahmed, K. A., Ali, M. Y., and Alvi, F. S., "Mixing Characteristics of Active Microjet-Based Actuators in a Supersonic Backward-Facing Step Flow," *AIAA Paper* 2011-0309. 2011.